3D fluid–structure interaction simulation of an hydrofoil at low Reynolds number

Fabien Salmon, Ludovic Chatellier

Journal of Fluids and Structures 111 (2022) 103573

Contents lists available at ScienceDirect

Journal of Fluids and Structures

journal homepage: www.elsevier.com/locate/jfs

3D fluid–structure interaction simulation of an hydrofoil at low Reynolds number

Fabien Salmon *, Ludovic Chatellier

Institut Pprime, CNRS - Université de Poitiers - ISAE-ENSMA, UPR 3346, Poitiers, France

ARTICLE INFO

Article history:
Received 28 August 2021
Received in revised form 16 January 2022
Accepted 30 March 2022
Available online 22 April 2022

Keywords:
CFD
Vortex-induced vibration
Lock-in
Strong coupling

ABSTRACT

Understanding the interaction between wings and fluids is of great interest in many fields such as aeronautics, wind turbines, civil engineering, naval and industrial domain, among others. To improve our knowledge, scientists have conducted more and more theoretical studies with numerical simulation. Due to the high complexity of the coupled phenomena leading to time-consuming fluid–structure interaction simulations, the overwhelming majority of these studies are restricted to two dimensions. Here, we present the full three-dimensional fluid–structure simulation of a foil in water. A deformable NACA 0015 wing, at 15° angle of attack, undergoes a $1\,m.s^{-1}$ flow in a water tunnel. We handle the simulation with free open-source software: OpenFOAM (fluid), CalculiX (solid) and preCICE (fluid–structure coupling). An implicit coupling is considered. The access to high-performance computing facilities allows us to run a Delayed-Detached-Eddy Simulation (DDES) based on a 15-million-cell mesh resolving the boundary layer on the wing. We also develop a meshing tool based on free software and Python scripts to facilitate the meshing process of wings or any shape in rectilinear geometries (2D and 3D). Then, we manage a thorough numerical investigation of the 3D phenomena involved in this fluid–structure problem. In particular, we reproduce the vortex-induced vibration process and observe the same fundamental frequency for the vortex shedding, the wing displacement oscillation and the lift and drag coefficients. Thus, we evidence that wing oscillatory displacements, of the order of 0.1% of the chord only, significantly affect the behavior of the flow.

1. Introduction

Fluid–structure interaction (FSI) is the study of the mutual effects between deformable structures and a surrounding fluid. This topic is of great interest when, for instance, the stress undergone by a solid or its displacement must be known for mechanical dimensioning. Among others, turbines (Trivedi and Cervantes, 2017; Müller et al., 2017), bridges (Szabó and Györgyi, 2009), buildings (Huang et al., 2013) or wings (Nakata and Liu, 2012; Genç et al., 2020) require the investigation of fluid–structure interactions. Today, this field is widely studied through numerical simulation. This branch is based on the numerical resolution of the equations governing physical phenomena (Takizawa et al., 2012) and often needs high performance computing. For the simulations to remain reasonably time-consuming, many authors have investigated fluid–structure interactions in two dimensions (Mahboubidoust et al., 2017; van Opstal et al., 2015; Güner et al., 2019). With increasing computing performances, scientists start to manage 3D investigations. A first approach to simulate 3D FSI

* Corresponding author.
E-mail address: Fabien.Salmon@u-bordeaux.fr (F. Salmon).

https://doi.org/10.1016/j.jfluidstructs.2022.103573

is one-way simulation (only fluid towards solid). For instance, Wang et al. (2016) present the interaction between a blade and air. Another approach consists in a genuine FSI coupling such as in Gan et al. (2017) where Gan et al. study a high Mach number flow around a deformable airfoil. Šekutkovski et al. (2016) also investigate the 3D interaction between an airfoil and air. It is worth noting that both papers concern interaction with air, which needs relatively low time-consuming numerical methods in comparison with denser fluids.

The simulation of fluid–structure interaction can be performed with different approaches. The monolithic approach (Michler et al., 2004) requires the resolution of only one set of equations encompassing the fluid and solid equations. This technique does not require any coupling between independent codes and only one solver is needed. Despite the inherent numerical stability and accuracy of this method, it is not widely adopted in literature because such a time-consuming resolution demands significant computational resources. The partitioned method (Matthies and Steindorf, 2003) is based on two software codes (fluid and structure) associated with a coupling interface. Two sets of equations are thus solved independently. This popular procedure leads to stability issues but can solve quite large problems within a reasonable time.

Our study is based on the partitioned approach and the use of three open-source software codes: OpenFOAM (OpenFOAM), CalculiX (Dhondt, 2021) and preCICE (Bungartz et al., 2016). OpenFOAM manages the fluid part of the simulation, CalculiX the solid part and preCICE handles the interface between both solvers. The partitioned method covers different approaches. The explicit (loosely coupled) way works fine provided that the fluid density is far smaller than the solid one (weak added mass effect). Many investigations are carried out with this time-efficient approach (De Nayer et al., 2018; Zhang and Xu, 2019). Typically, explicit coupling is stable and accurate with gases but not with liquids, like in Gan et al. (2017) and Šekutkovski et al. (2016). To overcome this matter, the implicit approach (strongly coupled) can be considered. In an implicit coupling, the fluid equations and the solid equations are solved several times per time step until convergence is attained. This method is very time-consuming but stable and is often used in literature (Martinez-Ferrer et al., 2018; Lee et al., 2017; Liu et al., 2017).

Here, we present the 3D simulation of the interaction between a foil and the surrounding water in a tunnel. The Reynolds number is equal to 8.10^4 and the angle of attack of the foil is 15°. This study extends the previous experimental work reported by Acher et al. (2019) and falls within the European H2020 HOMER project (Holistic Optical Metrology for Aero-Elastic Research) which concerns the study of fluid–structure interactions from both experimental and numerical points of view.

First, the numerical methods employed in the FSI simulation are detailed. The fluid and the solid resolution are described as well as the mesh motion in the fluid simulation. The coupling between CalculiX and OpenFOAM, which relies on the Quasi-Newton inverse least squares method, is explained. Second, we present a custom-made meshing tool based on existing free software. This code consists of several Python scripts and makes the best use of GMSH (Geuzaine and Remacle, 2009), cfMesh (cfMesh, 2020) and snappyHexMesh (snappyHexMesh, 2020). It allows users to automatically mesh the shell of a wing within a surrounding medium, including boundary layers. Other shapes can also be meshed since this tool can take CAD files as inputs. It is now made available online (pyMeshFOAM, 2021). Finally, the results of the simulation are discussed. The phenomena resulting from the interaction between the flow and the elastic wing are particularly studied. A thorough investigation of the frequencies that are characteristic of the fluid–structure interactions is presented.

2. Numerical methods

The fluid–structure simulation presented in Section 4 is performed with the software codes OpenFOAM, CalculiX and preCICE respectively used for fluid simulation, solid simulation and interfacing. This section addresses the description of the mathematical methods involved in each of them.

2.1. Fluid

2.1.1. Equations

This study concerns the interactions between a wing and water. Therefore, OpenFOAM solves the incompressible Navier–Stokes equations (1) with the finite volume method.

$$\begin{aligned} \nabla.u &= 0 \\ \frac{\partial u}{\partial t} + (u - u_\Omega).\nabla u &= -\frac{1}{\rho}\nabla P + (\nu + \nu_t)\,\Delta u \end{aligned} \tag{1}$$

where u is the fluid velocity, u_Ω is the grid velocity, ρ is the fluid density, P is the pressure, ν is the kinematic viscosity and ν_t is the eddy viscosity. The assessment of u_Ω depends on the adopted point of view. The Lagrangian approach corresponds to $u_\Omega = u$ while the Eulerian one is for $u_\Omega = 0$. Here, we adopt the Arbitrary Lagrangian–Eulerian (ALE) approach. The grid velocity is computed at each time step and depends on the interface motion.

2.1.2. ALE formulation

From the calculated displacement of the interface by the solid solver, the fluid mesh moves according to a diffusion equation. The displacement of each cell is diffused from the interface to the surrounding walls where there is no displacement. OpenFOAM thus solves

$$\nabla.\left(\gamma \nabla u_{\Omega}\right) = 0 \tag{2}$$

The diffusion coefficient γ is chosen to be inversely proportional to the second power of the distance from the interface.

2.1.3. Turbulence

This study is concerned by turbulence since a flow separation with vortex shedding is expected. Detached-eddy simulation (DES) (Spalart et al., 1997) combines the strengths from large-eddy simulation (LES) and unsteady Reynolds-averaged Navier–Stokes (RANS) for this kind of problem. The boundary layer is solved with the RANS modeling since LES would require a too refined mesh whereas far enough from the critical boundary, LES is activated since it better predicts large separation regions than RANS (Spalart, 2009). However, it has been found that this modeling is grid-dependent, which leads to early separation. To overcome this weakness, Spalart et al. (2006) improved the initial modeling to avoid the separation issue. Here, we adopted this turbulence modeling, called DDES (Delayed Detached-Eddy Simulation).

More particularly, the simulation is based on the RANS Spalart–Allmaras model which relies on the following equation

$$\frac{\partial \tilde{\nu}}{\partial t} + \nabla.\left(u\tilde{\nu}\right) = C_{b1}\tilde{S}\tilde{\nu} + \frac{C_{b2}}{\sigma}\nabla\tilde{\nu}.\nabla\tilde{\nu} + \frac{1}{\sigma}\nabla.\left(\left(\nu+\tilde{\nu}\right)\nabla\tilde{\nu}\right) - C_{w1}f_w\left(\frac{\tilde{\nu}}{d}\right)^2 \tag{3}$$

with $\tilde{\nu} = \frac{\nu_t}{f_{v1}}$, $\tilde{S} = \sqrt{2\Omega_{ij}\Omega_{ij}}$, $\Omega_{ij} = \frac{1}{2}\left(\frac{\partial u_i}{\partial x_j} - \frac{\partial u_j}{\partial x_i}\right)$, d the distance to the wall, $\sigma = 2/3$, $C_{b1} = 0.1355$, $C_{b1} = 0.622$ and $C_{w1} = 3.24$. The functions f_{v1} and f_w are defined in the original paper (Spalart et al., 2006). In the DDES formulation (Spalart et al., 2006), the distance to the wall is replaced by $\tilde{d} = d - f_d max\left(d - C_{DES}\Delta, 0\right)$ with $\Delta = \left(\Delta x \Delta y \Delta z\right)^{1/3}$ the filter size (in OpenFOAM), $C_{DES} = 0.65$, $C_{DES} = 0.65$, $r_d = \frac{\nu_t+\nu}{|\nabla u|(\kappa d)^2}$ and $\kappa = 0.41$ the Kármán constant.

When $d \ll \Delta$, $\tilde{d} \sim d$ so the turbulence model corresponds to Spalart–Allmaras (RANS). When $d \gg \Delta$, the model behaves in a Smagorinsky-like manner (LES).

2.1.4. Numerical schemes

With such a coupling, it is advised to choose a fixed time step. The simulation presented in Section 4 is based on $\Delta t = 10^{-5}$ s. This corresponds to a Courant number smaller than 0.5 in the fluid calculation. The second order upwind scheme is applied to solve the convection term in the momentum Eq. (1). It is worth noting that the TVD (Total Variation Diminishing) scheme in OpenFOAM appears not suitable for this term in our simulation. The diffusive term of this equation is treated with a linear approach. A TVD scheme is applied to the divergence term associated with the turbulence variable $\tilde{\nu}$. The temporal discretization is achieved with the second order backward scheme. The pressure equation is solved with the multigrid method GAMG (Geometric Algebraic MultiGrid). The other linear systems are solved with the preconditioned bi-conjugate gradient stabilized method. The preconditioner is calculated by the simplified diagonal-based incomplete LU method. The resolution of the incompressible Navier–Stokes equations is based on the PIMPLE algorithm implemented in OpenFOAM composed of two iterations of the PISO algorithm (Pressure Implicit with Splitting of Operator). For our simulation, five iterations are often needed to converge.

2.2. Solid

CalculiX manages the resolution of the equations governing the linear-elastic deformation of the wing. The code is based on the finite element method. These equations correspond to

$$\begin{aligned} &\rho\frac{\partial^2 d}{\partial t^2} + \nabla.\Sigma = 0 \\ &\Sigma = 2\mu\varepsilon + \lambda tr\left(\varepsilon\right) I \\ &\varepsilon = \frac{1}{2}\left(\nabla^T d + \nabla d\right) \end{aligned} \tag{4}$$

where d is the displacement, (μ, λ) are the Lamé parameters and I is the second rank unity tensor.

2.3. Coupling

An implicit coupling corresponds to the resolution of the fluid equations and then the solid equations several times per time step until convergence. Note that the mesh motion is also performed as many times as the equations are solved. This method is outlined in Fig. 1.

During the FSI loop, the interface displacement calculated by CalculiX is not directly imposed as the displacement in OpenFOAM at the next iteration. Instead, a coupling algorithm computes the interface displacement at iteration k+1 by

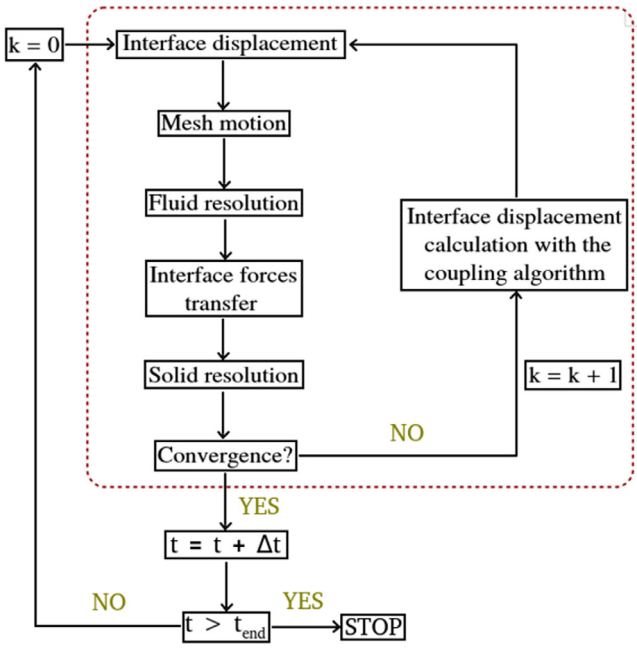

Fig. 1. Numerical process of an implicit fluid–structure interaction simulation.

solving a fixed point equation. Let us note ζ the operator that stands for the fluid solver and π the one for the structure equations. The displacement d is related to the stress σ by $\sigma = \zeta(d)$ and $d = \pi(\sigma)$. These relations lead to the fixed point equation $R(d) = d - \pi(\zeta(d)) = 0$ where R is a residual operator. In this study, this equation is solved with the IQN-ILS method (Quasi-Newton inverse least squares) (Degroote et al., 2009).

3. Numerical set-up

3.1. Test case

We present the simulation of the interaction between an elastic wing and a water flow. The NACA0015 hydrofoil is located in a 60 cm long tunnel which has a square cross-section of 23 cm (Fig. 2). The chord of the foil is 8 cm while its angle of attack is 15°. The wingtip is not straight but corresponds to a half circle shape joining the intrados to the extrados. The wingtip adds 6 mm to the length of the wingspan which is 14 cm without the wingtip. The material is assumed to be isotropic with a Young modulus equal to 3.5 GPa and a Poisson ratio of 0.3. Its density is 2170 kg/m^3. The flow velocity is 1 m s^{-1} which corresponds to a Reynolds number equal to 8.10^4.

The fluid–structure interaction simulation presented in Section 4 was performed with ten 2 × 24-cores Intel Skylake 2.7 GHz on the TGCC-CEA supercomputer Irene. The simulation of 0.05 s with the mesh described in the following section required ten days of calculation on these 480 cores. The time duration is based on the characteristic time of the fluid–structure interaction phenomena. The smallest frequency of vibration in the performed simulation is 60 Hz. The calculation time will allow us to compute three periods of this motion. It turns out to be enough to reach stationarity (Huang et al., 2019; Zeng et al., 2019).

3.2. Development of an automatized free meshing process

The consistency of the results of a simulation is directly linked with the mesh quality. However, achieving a quality mesh of a 3D shape within a surrounding medium, with refinements and boundary layers with commercial or open-source tools is still challenging. We propose an automatized numerical tool capable of meshing a 3D wing inside a box while making best use of existing free mesh generation codes. Both fluid and solid are meshed according to user parameters. All the Python scripts are available online as well as tutorials (pyMeshFOAM, 2021). In this section, we briefly describe the open-source code on the geometry of the test case while more details are provided in the source files and in the online user guide.

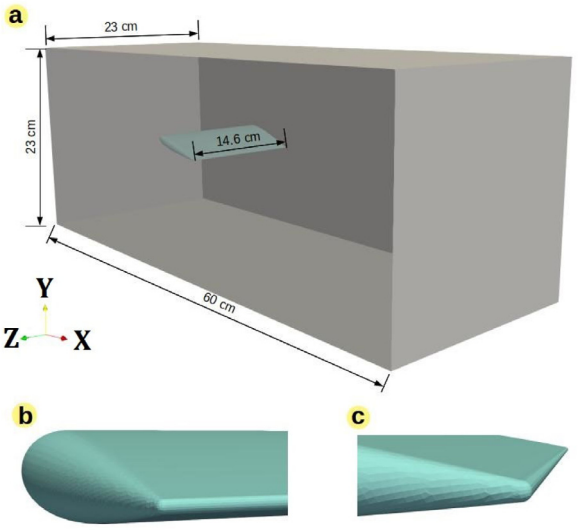

Fig. 2. (a) The geometry corresponds to a NACA 0015 profile in a water tunnel. (b) Zoom on the wingtip. (c) Zoom on the smoothed trailing edge.

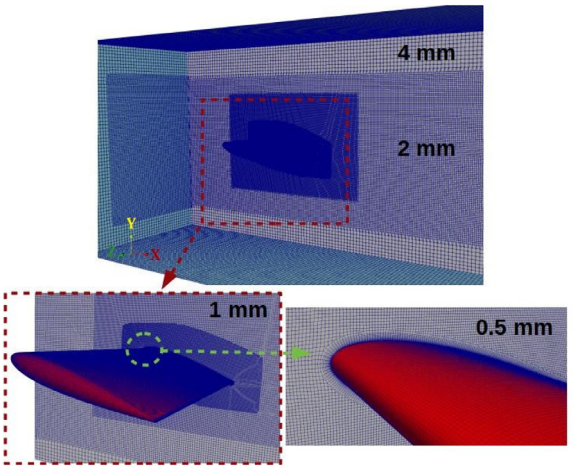

Fig. 3. Fluid mesh with the size of the cells in each zone. Zoom on the boundary layer mesh around the wing.

3.2.1. Fluid

Except the boundary layer, the mesh of the fluid is achieved with the free version of the meshing tool cfMesh. This version cannot mesh properly the boundary layers so this task is performed with the meshing tool snappyHexMesh natively provided in the OpenFOAM library. In this investigation, the mesh of the boundary layer is composed of 17 cells in the orthogonal direction to the wing. The exponential ratio is 1.15 while the first cell is designed to correspond to $y^+ \sim 1$. The mesh contains cells of different sizes: 0.25 mm at the trailing edge, 0.5 mm around the wing and then 1, 2 and 4 mm as we move away from the wing (Fig. 3). This corresponds to approximately 160 cells along the chord ($\frac{\Delta x}{chord} \sim 0.006$). The mesh consists of approximately 15 million cells. In parallel to an experimental validation of the model, we perform a mesh convergence study in Section 3.3.

The trailing edge is smoothed out to make the simulation more stable. Indeed, with a sharp edge, the mesh in this area is of bad quality (Fig. 4). Although the skewness and the orthogonality remain acceptable, the numerical simulation has trouble to converge to the solution of the physical problem. Fig. 4 displays the horizontal velocity field around the trailing edge of a 2D rigid NACA0015 profile with an angle of attack of 15° which experiences a $1\,m\,s^{-1}$ horizontal flow. The maximum velocity was expected to remain smaller than $2\,m\,s^{-1}$, which does not happen in our simulation ($>4\,m\,s^{-1}$). In addition, this discrepancy increases the computational cost of the resolution with more than five more PIMPLE iterations. The trailing edge smoothing avoids this issue, even with the mesh motion.

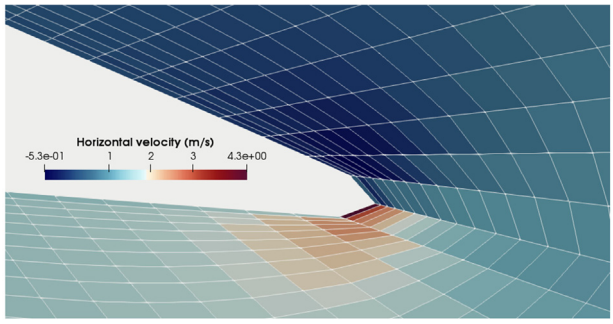

Fig. 4. Numerical instability leading to an overestimation of the velocity close to the trailing edge due to bad quality cells. Rounding up this part of the wing ensures a better quality mesh.

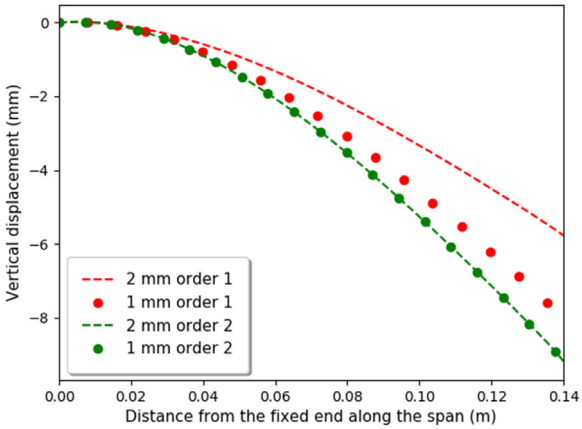

Fig. 5. Comparison for different meshes of the deflection at the leading edge of a NACA 0015 foil experiencing gravity and subject to a force of 10 N at $z = 14$ cm on the leading edge.

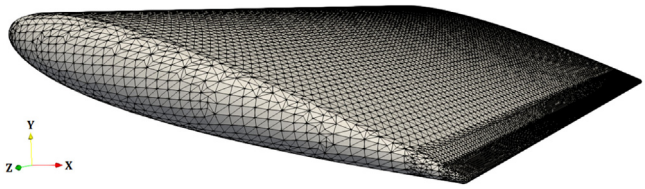

Fig. 6. Solid mesh of the hydrofoil composed of 70,000 elements.

3.2.2. Solid

The meshing process of the solid part is handled by GMSH (Geuzaine and Remacle, 2009). The algorithm is designed to make the nodes of the solid interface match with those of the fluid interface. This avoids interpolations between both interfaces during the exchange of data. Here, the fluid mesh is very refined near the wing so we do not consider this matching to decrease the mesh size of the solid wing. The output mesh file is automatically rewritten to make it suitable for CalculiX.

We perform here a grid convergence study on a test case based on the same NACA profile with four different meshes. The wing experiences gravity and a force of 10 N is applied on the point $z = 14$ cm at the leading edge. Linear and quadratic elements are considered as well as elements of 2 mm and 1 mm. Fig. 5 displays the comparison between the four configurations on the bending profile of the wing trailing edge.

The mesh composed of linear elements should be more refined to yield consistent results. However, quadratic elements of 1 or 2 mm lead to the same profile. The convergence is thus satisfied with quadratic elements of 2 mm. We made the choice of this mesh for the simulation. The size of the greatest elements is 2 mm while the element size is 0.5 mm at the trailing edge. The solid mesh is composed of approximately 70,000 quadratic elements (Fig. 6).

Table 1
Numerical lift and drag coefficients in the test case presented in Zheng et al. (2019) for three different meshes.

	Lift coefficient	Drag coefficient
Coarse mesh	0.73	0.1
Medium mesh	0.65	0.17
Fine mesh	0.62	0.2

3.3. Validation of the numerical model

Zheng et al. (2019) investigated the effect of alternating current and nanosecond plasma actuators on flow separation. In their study, they conducted an experiment on a NACA0015 airfoil configured until an angle of attack of 14° and subject to a Reynolds number equal to 6.3×10^4. The plasma actuators were not activated. The wing chord was 8 cm while the span measured 15.8 cm with a flat tip. The dimensions are thus very close to those of the wing in our simulation. The section of the tunnel is 0.16×0.16 m^2 and its length is 0.75 m. Note that there is no wall at the side of the wing tip which is open to the outside instead. The wing is thus less confined in the tunnel than in our test case.

For an angle of attack of 14°, they measured an averaged lift coefficient equal to 0.65 and a drag coefficient of 0.2.

We have reproduced this case numerically with several mesh discretizations. The first configuration corresponds to a coarse mesh looking like that of Fig. 3 where the cells are four times bigger (2 million cells). The medium mesh is composed of cells twice bigger (6 million cells) while the fine mesh approximately corresponds to Fig. 3 but with the Zheng et al. case (15 million cells). In the three cases, the boundary layer is meshed with the same characteristics (Section 3.2.1). Table 1 shows the calculated lift and drag coefficients in the three configurations.

The simulation based on the coarse mesh does not give a satisfactory drag coefficient (half the expected value). The medium mesh leads to the experimental lift coefficient but a finer mesh decreases its value. So the DDES modeling provides a lower lift coefficient (5%) than the measurement in Zheng et al. (2019). Concerning the drag coefficient, the simulation seems to converge to the experimental value provided by Zheng et al. Our model is thus relevant for this kind of study.

The deviation for the medium mesh might be considered small enough to be chosen in the FSI simulation. However, flow separation is difficult to predict and the interaction with the solid will modify a lot the drag and lift coefficients (see Section 4). Because we have access to a supercomputer sufficiently competitive to perform the FSI simulation with the finest mesh, we choose this configuration. Note that this discretization is consistent with the results obtained in Huck et al. (2019) where DDES of pre-stalled wings are studied. Huang et al. (2019) also chose a similar mesh for their FSI simulation, 150 cells along the chord (160 in our study).

4. Results and discussion

4.1. Establishment of the fluid circulation

We first perform the fluid simulation of a water flow around the rigid NACA 0015 hydrofoil during 2 s. The wing motion is thus avoided. This allows the establishment of the general flow pattern before making the fluid–structure interaction simulation which is more time-consuming. Fig. 7.a displays the vortex shedding structure through the iso-surface of the Q-criterion. One can see the leading edge vortices and the tip vortex which are well-known structures in this kind of flow (Clancy, 1975; Ginevsky and Zhelannikov, 2009; Green, 1995). The trailing edge vortices are also observed in the simulation. Fig. 7.b shows the velocity magnitude. The boundary layer is detached from the foil. This behavior was expected since the angle of attack is 15° which is greater than the critical angle in this configuration.

Fig. 8 displays the lift and drag coefficients during the fluid simulation. These coefficients vary significantly over one second and then stabilize. The full detachment of the boundary layer then takes approximately one second. This behavior thus supports the choice of a two-second simulation as an initial step for a fluid–structure interaction simulation. The lift coefficient after the transient part of the simulation is between 0.45 and 0.5 while the drag coefficient remains close to 0.2.

This allows us to consider that the general flow circulation around the NACA0015 hydrofoil is established after 2 s of simulation. The end of this fluid simulation is taken as the beginning of the FSI simulation.

4.2. Fluid–structure interaction

4.2.1. Effects of the fluid on the solid

4.2.1.1. Solid displacement. The strong coupling allows the calculation of the solid displacement. For each time step, four or five FSI loops have been needed to ensure the convergence of the simulation. We present in Fig. 9 the deflection of the wing at one-quarter of the chord 8 ms after the beginning when the displacement is maximal.

As expected, the vertical displacement is positive due to the pressure difference between the suction and pressure sides of the wing. The weight of the hydrofoil has low effect since the solid density is close to that of water.

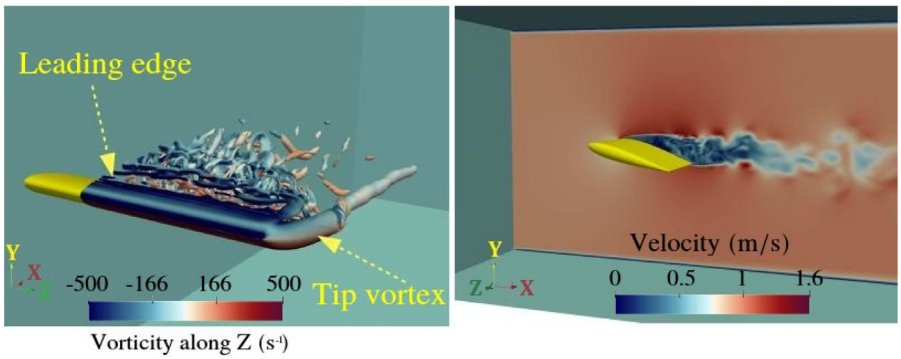

Fig. 7. Snapshots derived from the fluid simulation without any wing motion (2 s). (a) Iso-surface of the Q-criterion ($Q = 5 \times 10^3$) colored by the z-component of the vorticity. (b) Magnitude of the velocity in the plane $z = 7$ cm.. (For interpretation of the references to color in this figure legend, the reader is referred to the web version of this article.)

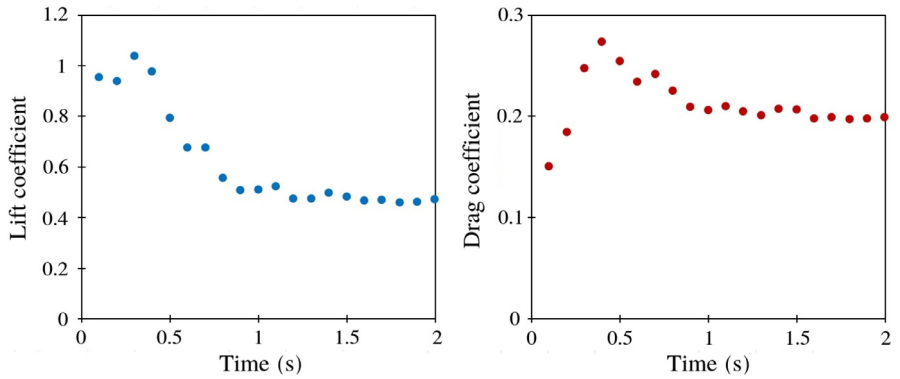

Fig. 8. Numerical lift and drag coefficients against time (NACA 0015, $Re = 8 \times 10^4$ and $\alpha = 15°$).

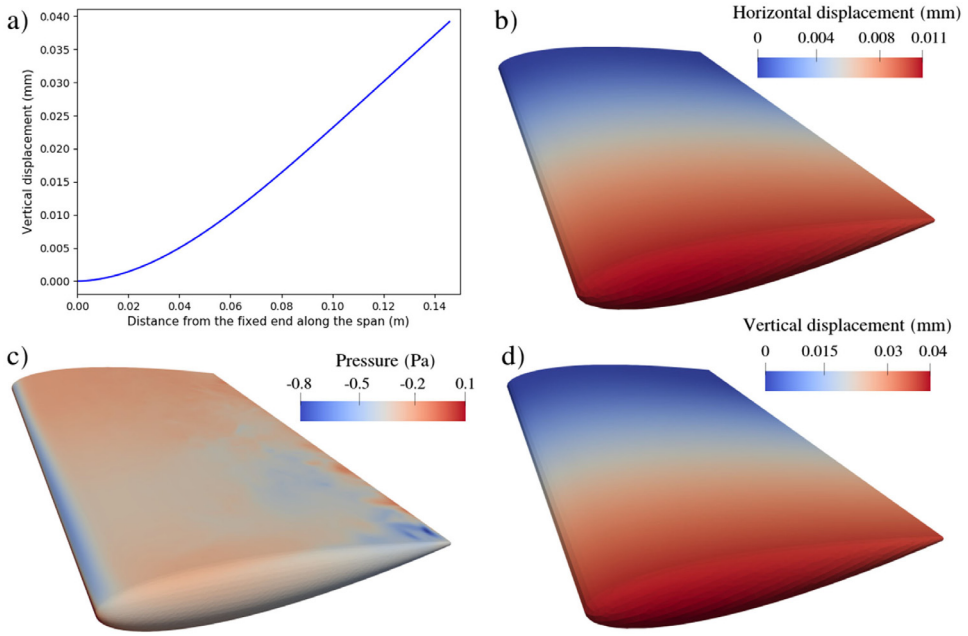

Fig. 9. (a) Deflection of the NACA 0015 foil at one-quarter of the chord after 8 ms. (b) Horizontal displacement of the wing after 8 ms. (c) Pressure field over the wing surface after 8 ms. (d) Vertical displacement of the wing after 8 ms.

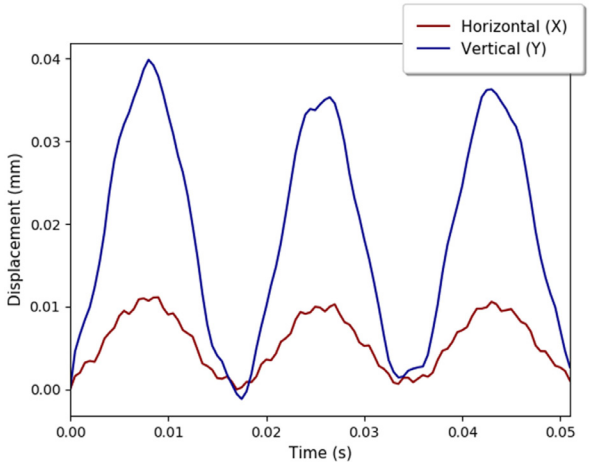

Fig. 10. Vertical and horizontal displacement of the leading edge of the wing at $z = 14$ cm against time.

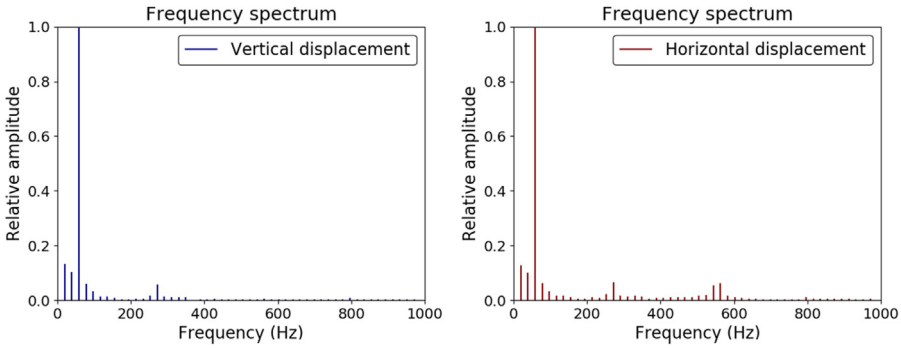

Fig. 11. Frequency spectra of the vertical and horizontal displacements of the leading edge of the wing at $z = 14$ cm.

The displacement corresponds to a classical bending profile. A third-order polynomial can describe the curve with a good correlation coefficient (0.99). This could have been expected since the pressure field applied on the wing has little dependence on the wingspan (z coordinate) except in the vicinity of the wing root and tip (Fig. 9c).

The torsion of the wing is weak. The deviation in the vertical displacement between the leading and the trailing edge remains smaller than 2.5 μm for a tip displacement of the order of 40 μm (Fig. 9d). This only corresponds to 6% of the vertical displacement. The torsion angle is approximately 1.8×10^{-3} degree. The torsion process is thus small in comparison with the bending one.

Fig. 10 displays the displacement of the leading edge of the foil at $z = 14$ cm (tip), where it reaches its maximum value, as a function of time.

The vertical displacement is between three and four times greater than the horizontal displacement which remains smaller than 0.01 mm most of time. The peak values for both directional displacements are met together. In addition, the same main oscillation frequency of 60 Hz is observed for both displacements. The frequency spectrum of both displacements is given in Fig. 11. A second mode of vibration of approximately 280 Hz also exists in the wing displacements. A third frequency ($\sim$ 560 Hz) appears only on the horizontal displacement.

We can compare these modes of vibration with those of the elastic wing. Fig. 12 displays the first three modes of vibration of the wing. The modes in vacuum are calculated with Calculix and the modes in water are calculated with the present FSI coupling, without fluid velocity. The first bending mode appears at 60 Hz in water. The added mass effect due to water decreases this natural oscillation frequency. The next mode of vibration of the wing is the torsion mode at 280 Hz. It corresponds to the frequency of 280 Hz in Fig. 11. The third frequency, observed only in the horizontal displacement (Fig. 11), corresponds to the first bending mode along Y (mode 3 in Fig. 12). The added-mass effect is smaller in this motion than in modes 1 and 2. The mass of fluid displaced during the bending motion along Y remains relatively weak due to the small thickness of the NACA0015 profile (6 mm), while in modes 1 and 2, the fluid displacement is directly linked with the chord (8 cm). This explains why this frequency does not appear in the frequency spectrum of the vertical displacement.

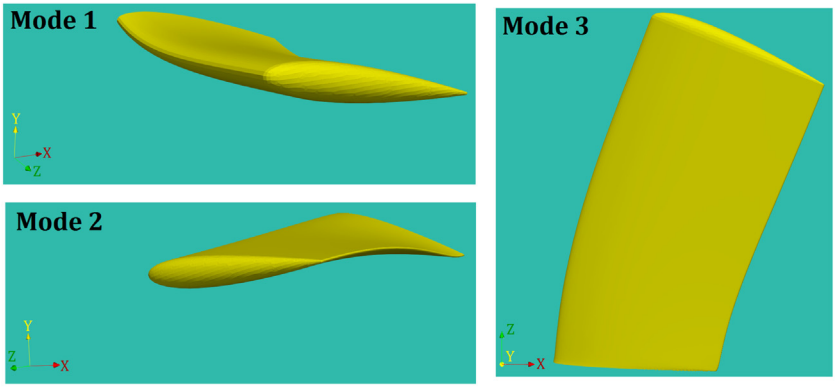

	Vacuum	Fluid	Mode of vibration
1	~100 Hz	~60 Hz	1st bending mode along X
2	~440 Hz	~280 Hz	1st torsion mode
3	~570 Hz	~570 Hz	1st bending mode along Y

Fig. 12. First three natural modes of vibration of the wing calculated by CalculiX.

We propose here different analytical calculations of the modes of vibration in water to substantiate the frequency predicted by the FSI simulation (Fig. 12). First, we applied the boundary element method (BEM), combined with the potential flow theory (Kramer et al., 2013), to the 2D NACA 0015 profile with an angle of attack of 15°. This approach allows us to compute the velocity potential around the wing φ_q ($q \in [1, 6]$ depending on the motion) and then to calculate the added-mass coefficient $CM_{pq} = \frac{-1}{c^2}\int_{Contour} \varphi_q \partial \frac{\varphi_p}{\partial n} dl$, where c is the chord and n is the unit vector orthogonal to the wing. The first bending mode corresponds to a vertical motion and is associated with $CM_{22} \sim 0.73$. The second bending mode is associated with $CM_{11} \sim 0.07$. From these coefficients, it is now possible to assess the frequency deviation when the solid is immersed in water $\nu_{water} = \frac{\nu_{vacuum}}{\sqrt{\left(1+\frac{\rho_{water}}{\rho_{wing}} CM\right)}}$. The second bending mode is thus not affected due to the low added-mass coefficient. Note that this is consistent with the analytical added-mass coefficient for an ellipse, equal to $\frac{b^2}{a^2}\pi$, which is very small when the semi-minor axis b is far smaller than the semi-major axis a. The first bending mode in water is estimated to be approximately 86 Hz, which is higher than the frequency calculated with the FSI simulation. The difference can stem from the inherent hypotheses of the potential flow theory, but also from the 2D assumption.

There exists an analytical solution for 3D plates with no angle of attack (Kramer et al., 2013). In the previous theoretical framework, the frequency difference between wings at 0° and 15° remains smaller than 1 Hz on the first bending mode. We thus assume that the angle, which remains weak, does not have a significant impact on the analytical added-mass coefficients. Note that the authors of Kramer et al. (2013) expect the analytical relations for plates to be representative for hydrofoils. The potential flow and strip theories lead to $CM_{1st,bending} = \frac{\pi}{4}\frac{b}{t}$ and $CM_{torsion} = \frac{3\pi}{32}\frac{b}{t}\frac{b^2}{b^2+t^2}$, where b corresponds to the width of the plate and t to the thickness. The calculation with the chord as b and the average thickness of NACA0015 profiles (approximately 10% of the chord) as t gives $\nu_{water,1st,bending} \sim 50$ Hz and $\nu_{water,torsion} \sim 290$ Hz. These estimations are close to the modes of vibration calculated with the FSI simulation.

4.2.1.2. Vortex-induced vibration. The first mode of vibration of the wing actually results from the shear-layer vortices. These structures probably derived from the Kelvin–Helmholtz instability and correspond to vortices in the separated shear-layer of a hydrofoil for instance. The vortex shedding frequency calculated in our simulation is in the same range as the experimental measurements achieved on similar cases (Yarusevych and Sullivan, 2006; Yarusevych et al., 2009). Like for the solid displacement, this frequency is approximately 60 Hz. This frequency leads to a chord-based Strouhal number equal to $St = \frac{fc}{U_\infty} \sim 4.8$. This order of magnitude is consistent with the Strouhal numbers associated with shear-layer vortices obtained experimentally on NACA0018 and NACA0025 profiles at $Re \sim 10^5$ and angles of attack between 10 and 15° (Yarusevych et al., 2005; Lambert and Yarusevych, 2019; Boutilier and Yarusevych, 2012).

Fig. 13 displays the pressure field in the plane $z = 7$ cm. The local pressure minima regions, which correspond to vortices, are pointed out with arrows. In 50 ms, one can observe the creation of three vortices in the separated shear-layer.

The vibration of the wing at the same frequency as that of the vortex shedding is a well-known phenomenon which has been observed experimentally (Ducoin et al., 2012). A second phenomenon occurs in our FSI simulation. As shown, the first bending mode of the structure is close to 60 Hz (Section 4.2.1.1). Thus, there is synchronization between this mode and the vortex-shedding frequency. This well-known phenomenon corresponds to lock-in (Zhang et al., 2015; Bourguet et al., 2011; Han et al., 2021). It precisely occurs when both frequencies are close to each other.

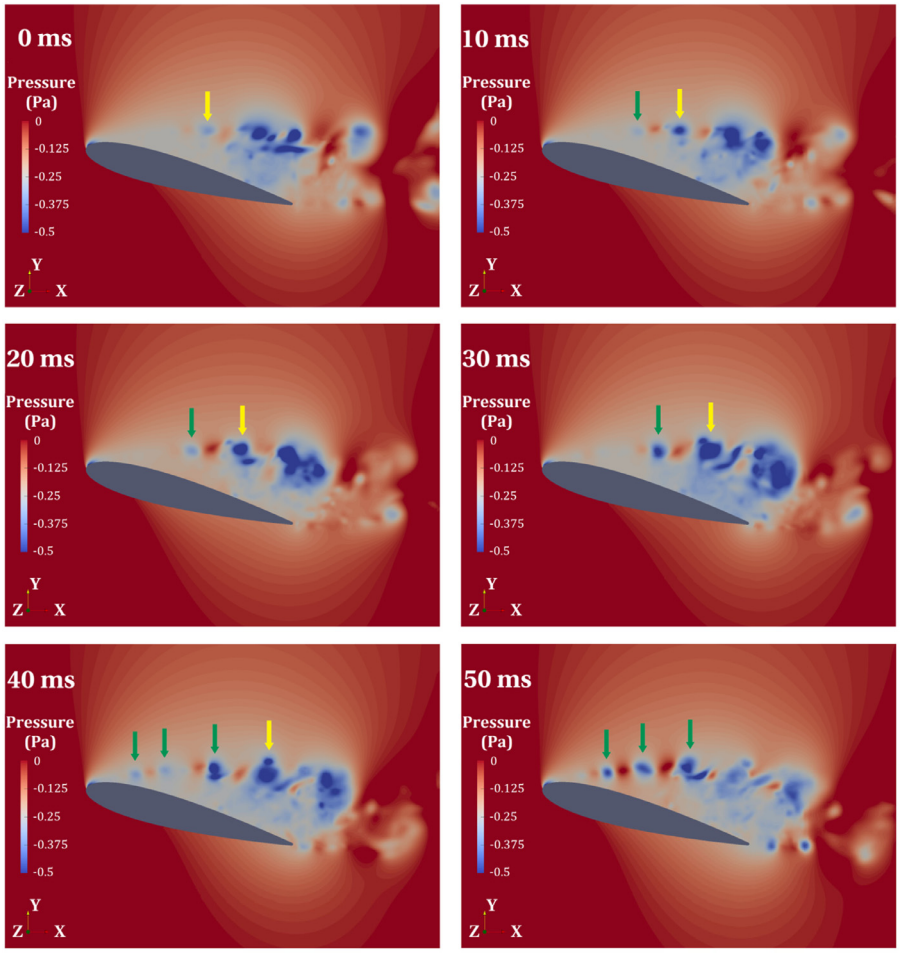

Fig. 13. Numerical pressure field in the $z = 7$ cm section at different times. The yellow arrow labels a vortex existing at the beginning of the FSI simulation while the green arrows correspond to new vortices. (For interpretation of the references to color in this figure legend, the reader is referred to the web version of this article.)

Moreover, like us, Ducoin et al. (2012) also observed other vibration modes (torsion and bending) of the solid in their frequency spectra.

4.2.2. Effects of the solid on the fluid

The displacement of the wing is rather low but is achieved fast. For instance, during the first 10 ms, the vertical displacement of the wing is 0.04 mm. This leads to an average velocity of 4 mm s^{-1} and a dynamic pressure of the order of 10^{-2} Pa. In this kind of problem, the maximal fluid pressure is of order 10^{-1} Pa. Thus, despite the weak value of the wing displacement, it has a non-negligible impact on the pressure in the fluid. Fig. 14 displays the initial pressure field and then the pressure difference between the fluid (rigid wing) and FSI simulations at different times around the hydrofoil at $z = 7$ cm.

As expected, the pressure difference is about 10^{-2} Pa due to the wing displacement. The sign of the difference upper and lower the wing mostly depends on the direction of its displacement. The greatest differences appear in the vortices, in the separated shear-layer and the wake behind the trailing edge. This was also expected since they correspond to local minima of pressure. Thus, in absolute terms, the pressure difference is greater in the vortices.

It is worth noting that the displacement of the wing does not impact significantly the vortex shedding frequency. Indeed, the locations of the shear-layer vortices seem to be the same in Fig. 14, 50 ms after the onset of the FSI simulation. Otherwise, distinctive contours in the pressure field forming the shear-layer vortices would not be observable. No location difference being observable, the difference of the shear-layer vortices frequency between the fluid and FSI simulations is necessarily smaller than 1 Hz.

The deviation in the pressure field between upper and lower the wing impacts the lift and drag coefficients. Since it results from the displacement of the wing, one can anticipate an oscillation of these coefficients with a frequency of 60 Hz. Fig. 15 compares the numerical lift and drag coefficients of both the fluid (rigid wing) and the FSI simulations.

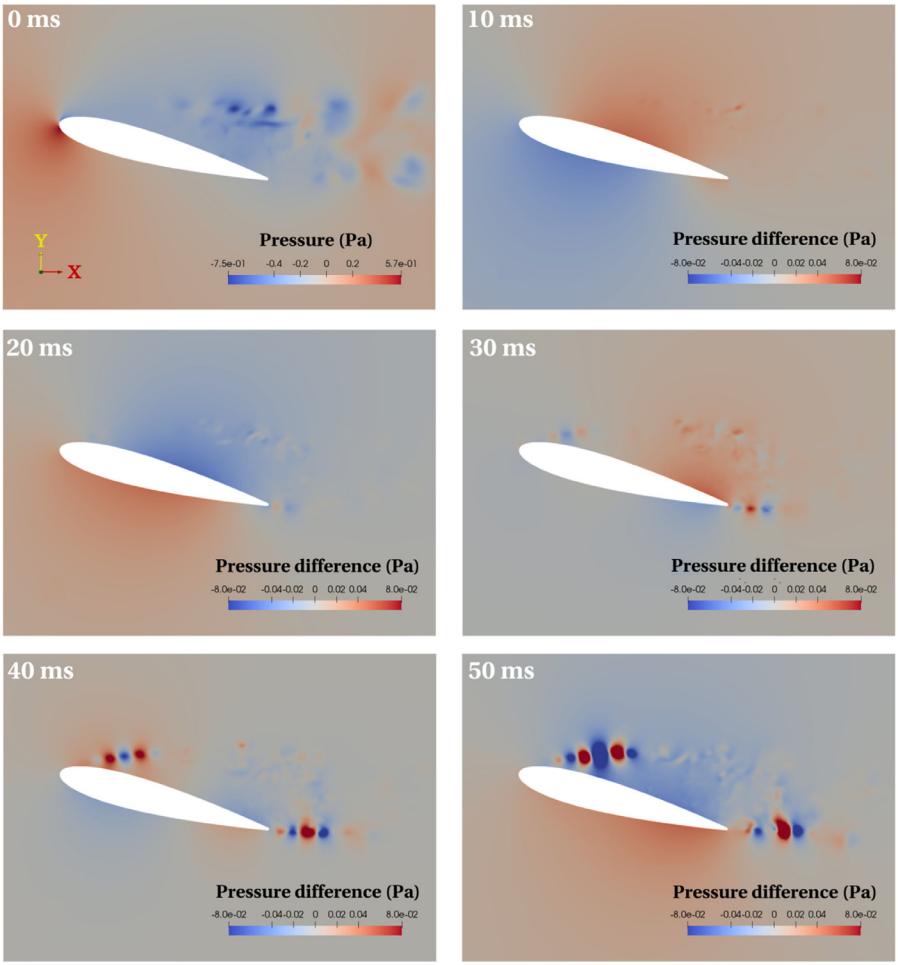

Fig. 14. Pressure field at initial time and difference of pressure between the fluid and the FSI simulations ($P_{fluid} - P_{FSI}$) in the $z = 7$ cm section.

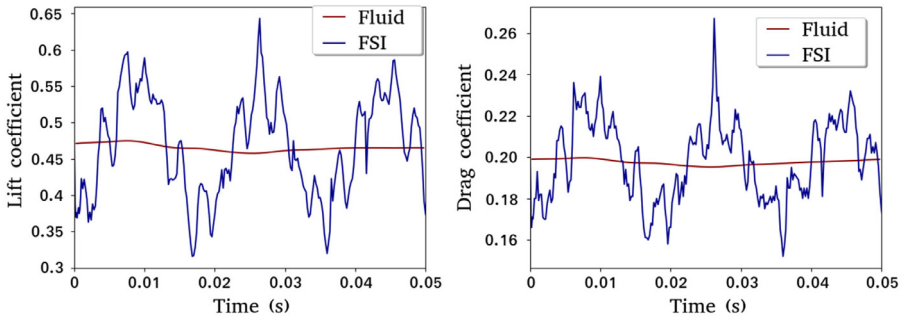

Fig. 15. Numerical lift and drag coefficients for the fluid and the FSI simulations at $z = 7$ cm against time (NACA 0015, $Re = 8 \times 10^4$ and $\alpha = 15°$).

The numerical coefficients present the intended behavior. The oscillations match those of the wing displacements while a rigid wing entails almost constant coefficients over 0.05 s. Without any wing motion, the shear-layer vortices do not impact a lot the pressure field close to the wing, and the corresponding frequency is thus not involved in the coefficients oscillation. Drag and lift coefficients rather oscillate with the vortices created behind the wing that form a Von Karman vortex street (Menon and Mittal, 2020).

Fig. 16 displays the frequency spectra of the drag and lift coefficients.

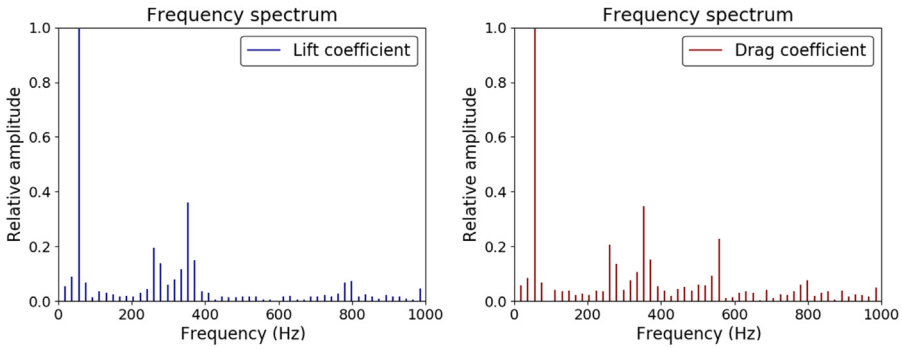

Fig. 16. Frequency spectra of the lift and drag coefficients over 0.05 s.

The frequency spectra of the displacements are similar to those of the coefficients. Both the 60 and 280 Hz appear in Fig. 16. The drag coefficient also presents a 560 Hz mode of vibration like the horizontal displacement. It was expected to impact only drag since lift is vertical.

A frequency of approximately 350 Hz ($St \sim 28$) also appears in Fig. 16 while there is no peak at this value in Fig. 11. Thus, this frequency does not stem from the solid motion but from fluid. Since the frequency does not match any natural frequencies of the wing, its displacement is weakly impacted by this load. The amplitude of the displacement is then lower at 350 Hz than at the modes of vibration. This frequency does not appear without solid motion so, even if it originates from fluid, it corresponds to a fluid–structure interaction phenomenon.

Conclusion

In order to challenge the numerical simulation of fluid–structure interactions, we carried out the three-dimensional FSI simulation of a NACA 0015 hydrofoil at moderate Reynolds number (8×10^4). The simulation was achieved by three free open-source software codes: OpenFOAM, CalculiX and preCICE. The fluid modeling was based on a DDES turbulence model and the solid computations used linear elasticity. The fluid–structure interaction required an implicit coupling for the simulation to remain numerically stable. To achieve an accurate simulation, we used a refined fluid mesh (15 million cells) to be able to resolve the boundary layer around the wing. Both features led to a very time-consuming FSI simulation which was run on 480 cores in ten days.

The meshing process with the available tools being sensitive for fine meshes, we have built an automatized meshing tool dedicated to shapes within rectilinear boxes based on Python scripts and free meshing software. The objective of this code is to facilitate the meshing process and optimize the mesh quality for OpenFOAM users. Note that the solid meshing process can also be automatically achieved in the case of a fluid–structure interaction simulation.

The numerical simulation leads to the expected behavior already highlighted experimentally. The frequencies inherent to the physical phenomena involved in such a fluid–structure interaction problem have been reproduced. The fundamental mode of vibration of the wing (60 Hz) corresponds to the shear-layer vortices frequency. Because the first bending mode of vibration of the wing is close to this value, we have observed the lock-in phenomenon. The natural frequency of the wing and the shear-layer vortices frequency have synchronized. The frequency spectrum of the wing displacement has presented other frequencies. In particular, the natural modes of vibration of the elastic wing (torsion, bending) have taken part in the wing motion.

The fast wing displacement has then affected the drag and lift coefficients due to high modifications of pressure above and below the wing. The characteristic frequencies appearing in the frequency spectra of the displacements are also in the spectra of the coefficients. Note that a frequency characteristic of a fluid phenomenon also affects the lift and drag coefficients without impacting much the wing displacement since it does not match any natural frequencies of the solid. The wing displacement, which has remained smaller than 40 μm, has still modified the lift coefficient up to 40%. Due to high pressure variations, the use of a strong coupling between fluid and solid was thus justified despite the weak wing displacement.

Based on a 3D fluid–structure interaction with strong coupling, we have therefore reproduced numerically the following pattern: the shear-layer vortices have made the wing vibrate which has locally modified pressure around it and has increased the fluctuations of the lift and drag coefficients.

In future work, this FSI simulation will be extended to a rotating elastic wing, based on the same software codes. Being embedded in the HOMER project, this will also take part in a data assimilation framework.

CRediT authorship contribution statement

Fabien Salmon: Writing – original draft. **Ludovic Chatellier:** Writing – review & editing.

Declaration of competing interest

The authors declare that they have no known competing financial interests or personal relationships that could have appeared to influence the work reported in this paper.

Acknowledgments

This project has received funding from the European Research Council (ERC) under the European Union's Horizon 2020 research and innovation programme, project HOMER: Holistic Optical Metrology for Aero-Elastic Research (grant agreement No 648161).

The computational work was granted access to the HPC resources of TGCC under the allocation *2021-A0092A10954* made by GENCI

References

Acher, G., Thomas, L., Tremblais, B., Gomit, G., Chatellier, L., David, L., 2019. Simultaneous measurements of flow velocity using tomo-PIV and deformation of a flexible wing. In: 13th International Symposium on Particle Image Velocimetry (ISPIV2019), July 22-24, Munich, Germany.

Bourguet, R., Karniadakis, G.E., Triantafyllou, M.S., 2011. Lock-in of the vortex-induced vibrations of a long tensioned beam in shear flow. J. Fluids Struct. 27, 838–847.

Boutilier, M.S.H., Yarusevych, S., 2012. Separated shear layer transition over an airfoil at a low Reynolds number. Phys. Fluids 24, 084105.

Bungartz, H.-J., Lindner, F., Gatzhammer, B., Mehl, M., Scheufele, K., Shukaev, A., Uekermann, B., 2016. preCICE - A fully parallel library for multi-physics surface coupling. Comput. & Fluids 141, 250–258.

2020. cfMesh. http://cfmesh.com.

Clancy, L.J., 1975. Aerodynamics. Wiley.

De Nayer, G., Apostolatos, A., Wood, J.N., Bletzinger, K.U., Wüchner, R., Breuer, M., 2018. Numerical studies on the instantaneous fluid–structure interaction of an air-inflated flexible membrane in turbulent flow. J. Fluids Struct. 82, 577–609.

Degroote, J., Bathe, K.-J., J., Vierendeels, 2009. Performance of a new partitioned procedure versus a monolithic procedure in fluid–structure interaction. Comput. Struct. 87, 793–801.

Dhondt, G., 2021. CalculiX, http://www.calculix.de/.

Ducoin, A., Astolfi, J.A., Gobert, M.L., 2012. An experimental study of boundary-layer transition induced vibrations on a hydrofoil. J. Fluids Struct. 32, 37–51.

Gan, J., Im, H.-S., Chen, X.-Y., Zha, G.-C., Pasiliao, C.L., 2017. Delayed detached eddy *simulation* of wing flutter boundary using high order schemes. J. Fluids Struct. 71, 199–216.

Genç, M.S., Açıkel, H.H., Koca, K., 2020. Effect of partialflexibility over both upper and lower surfaces toflow overwind turbine airfoil. Energy Convers. Manage. 219, 113042.

Geuzaine, C., Remacle, J.-F., 2009. Gmsh: a three-dimensional finite element mesh generator with built-in pre- and post-processing facilities. Internat. J. Numer. Methods Engrg. 79 (11), 1309–1331.

Ginevsky, A.S., Zhelannikov, A.I., 2009. Vortex Wakes of Aircrafts. Springer.

Green, S.I., 1995. Wing tip vortices. In: Green, S.I. (Ed.), Fluid Vortices. Fluid Mechanics and its Applications, Vol. 30. Springer, Dordrecht.

Güner, H., Thomas, D., Dimitriadis, G., Terrapon, V.E., 2019. Unsteady aerodynamic modeling methodology based on dynamic mode interpolation for transonic flutter calculations. J. Fluid Struct. 84, 218–232.

Han, L., Wei, D., Wang, Y., Zhang, X., 2021. Vortex-induced vibration mechanism of the NACA 0012 airfoil based on a method of separating disturbances. J. Sound Vib. 501, 116044.

Huang, S., Li, R., Li, Q.S., 2013. Numerical simulation on fluid–structure interaction of wind around super-tall building at high reynolds number conditions. Struct. Eng. Mech. 46 (2), 197–212.

Huang, Z., Xiong, Y., Xu, Y., 2019. The simulation of deformation and vibration characteristics of a flexible hydrofoil based on static and transient FSI. Ocean Eng. 182, 61–74.

Huck, V., Morency, F., Beaugendre, H., 2019. Grid study for delayed detached eddy-simulation's grid of a pre-stalled wing. In: CASI Aero 2019 - Canadian Aeronautics and Space Institute's AERO 2019 Conference, Laval, Canada.

Kramer, M.R., Liu, Z., Young, Y.L., 2013. Free vibration of cantilevered composite plates in air and in water. Compos. Struct. 95, 254–263.

Lambert, A., Yarusevych, S., 2019. Effect of angle of attack on vortex dynamics in laminar separation bubbles. Phys. Fluids 31, 064105.

Lee, A.H., Campbell, R.L., Craven, B.A., Hambric, S.A., 2017. Fluid–structure InteractionSimulation of vortex-InducedVibration of a flexible hydrofoil. J. Vib. Acoust. 139 (4), 041001.

Liu, Y., Xiao, Q., Incecik, A., Peyrard, C., Wan, D., 2017. Establishing a fully coupled CFD analysis tool for floating offshore wind turbines. Renew. Energy 112, 280–301.

Mahboubidoust, A., Ramiar, A., Darde, M., 2017. Investigation of steady plasma actuation effect on aerodynamic coefficients of oscillating *airfoil* at low Reynolds number. Theor. Appl. Mech. Lett. 7, 185–198.

Martinez-Ferrer, P.J., Qian, L., Ma, Z.H., Causon, D.M., Mingham, C.G., 2018. An efficient finite-volume method to study the interaction of two-phase fluid flows with elastic structures. J. Fluids Struct. 83, 54–71.

Matthies, H.G., Steindorf, J., 2003. Partitioned strong coupling algorithms for fluid–structure interaction. Comput. Struct. 81 (8-11), 805–812.

Menon, K., Mittal, R., 2020. Aerodynamic characteristics of canonical airfoils at low reynolds numbers. AIAA J. 58 (2), 977–980.

Michler, C., Hulshoff, S.J., van Brummelen, E.H., de Borst, R., 2004. A monolithic approach to fluid–structure interaction. Comput. & Fluids 33 (5–6), 839–848.

Müller, A., Favrel, A., Landry, C., Avellan, F., 2017. Fluid–structure interaction mechanisms leading to dangerous power swings in francis turbines at full load. J. Fluids Struct. 69, 56–71.

Nakata, T., Liu, H., 2012. A fluid–structure interaction model of insect flight with flexible wings. J. Comput. Phys. 231 (4), 1822–1847.

2021. https://openfoam.org/.

2021. pyMeshFOAM. https://github.com/FabienSalmon/pyMeshFOAM.

Šekutkovski, B., Kostić, I., Simonović, A., Cardiff, P., Jazarević, V., 2016. Three-dimensional *fluid–structure interaction simulation* with a hybrid RANS–LES turbulence model for applications in transonic flow domain. Aerosp. Sci. Technol. 49, 1–16.

2020. snappyHexMesh. https://openfoam.org/?s=snappyhexmesh.

Spalart, P.R., 2009. Detached-eddy simulation. Annu. Rev. Fluid Mech. 41, 181–202.

Spalart, P.R., Deck, S., Shur, M.L., Squires, K.D., Strelets, M.K., Travin, A., 2006. A new version of detached-eddy simulation, resistant to ambiguous grid densities. Theor. Comput. Fluid Dyn. 20, 181–195.
Spalart, P.R., Jou, W.-H., Strelets, M., Allmarasm, S.R., 1997. Comments on the feasibility of LES for wings, and on a hybrid RANS/LES approach. In: First AFOSR International Conference on DNS/LES, Ruston, Louisiana.
Szabó, G., Györgyi, J., 2009. Three-dimensional fluid-structure interaction analysis for bridge aeroelasticity. In: Proceedings of the World Congress on Engineering and Computer Science 2009 Vol IIWCECS 2009, October 20-22, San Francisco, USA.
Takizawa, K., Tezduyar, T., Bazilevs, Y., 2012. Computational Fluid-Structure Interaction: Methods and Applications. In: Wiley Series in Computational Mechanics.
Trivedi, C., Cervantes, M.J., 2017. Fluid–structure interactions in Francis turbines: A perspective review. Renew. Sustain. Energy Rev. 68, 87–101.
van Opstal, T., Fonn, E., Holdahl, R., Kvamsdal, T., Kvarving, A.M., Mathisen, K.M., Nordanger, K., Okstad, K.M., Rasheed, A., Tabib, M., 2015. Isogeometric methods for CFD and FSI-*Simulation* of flow around turbine blades. Energy Procedia 80, 442–449.
Wang, L., Quant, R., Kolios, A., 2016. Fluid structure interaction modelling of horizontal-axis wind turbine blades based on CFD and FEA. J. Wind Eng. Ind. Aerodyn. 158, 11–25.
Yarusevych, S., Kawall, J.G., Sullivan, P.E., 2005. Airfoil performance at low Reynolds numbers in the presence of periodic disturbances. ASME: J. Fluids Eng. 128 (3), 587–595.
Yarusevych, S., Sullivan, P.E., 2006. Coherent structures in an airfoil boundary layer and wake at low Reynolds numbers. Phys. Fluids 18, 044101.
Yarusevych, S., Sullivan, P.E., Kawall, J.G., 2009. On vortex shedding from an airfoil in low-Reynolds-number flows. J. Fluid Mech. 632, 245–271.
Zeng, Y., Yao, Z., Gao, J., Hong, Y., Wang, F., Zhang, F., 2019. Numerical investigation of added mass and hydrodynamic damping on a blunt trailing edge hydrofoil. J. Fluids Eng. 141 (8), 081108.
Zhang, W., Xintao, L., Zhengyin, Y., Jiang, Y., 2015. Mechanism of frequency lock-in in vortex-induced vibrations at low Reynolds numbers. J. Fluid Mech. 783, 72–102.
Zhang, Z., Xu, F., 2019. Added mass and damping effects on vibrating bridge decks in still air. J. Wind Eng. Ind. Aerodyn. 191, 227–238.
Zheng, J.G., Cui, Y.D., Khoo, B.C., 2019. A comparative study of alternating current and nanosecond plasma actuators in flow separation control. Int. J. Heat Mass Transfer 135, 1097–1117.